Approximating Simulated Stochastic Gravitational Wave Background BBHs with Broken Splines and Power Laws

Author: Taylor Knapp[1]
Mentors: Patrick Meyers[2], Arianna Renzini[2]
[1] *Brown University, Providence, RI, U.S.*
[2] *California Institute of Technology, Pasadena, CA, U.S.*
(Dated: September 22, 2022)

The Stochastic Gravitational Wave Background (SGWB) is usually assumed to be the combination of assumed isotropic, stationary, unpolarized, and Gaussian sources of gravitational waves. We expect a large contribution by neutron star and black hole binaries to this unresolved signal. Current LIGO detectors are not sensitive enough to the SGWB strain regime but we anticipate future observing runs to have the required sensitivity to detect the SGWB. The promise of future detectors registering the SGWB requires the introduction of detection and fitting algorithms to understand future observation results. A Reverse Jump Markov Chain Monte Carlo (RJMCMC) algorithm permits us to probe the fitting parameters for SGWB signals via spline and power law fittings. We present an RJMCMC fitting algorithm named Westley for this purpose. The versatility of the RJMCMC can be applied to the astrophysical case of recovering the energy density spectra based on injected mass distributions and merger rates for binary black hole mergers (BBHs). Accurately fitting the SGWB profiles and parametrizing profiles via spline and broken power laws will aid in identifying various components of the SGWB in data from upcoming LIGO observing runs.

I. INTRODUCTION

Gravitational waves are perturbations of the spacetime manifold expressed by the metric tensor $g_{\mu\nu}$ [10]. We are able to detect these fluctuations of space and time as strain, or change in length per unit length. This strain is detected by ground-based interferometers; two of such detectors are LIGO Hanford Observatory (LHO) and LIGO Livingston Observatory (LLO). This style of interferometer involves a laser split in two orthogonal directions and then recombined. These beams reflect off mirrors and coherently return to the source. When a gravitational wave passes, it strains the arms of the detector. This causes the light beams to move out of phase with one another, and so when the beams are recombined the resulting change in the interference pattern is evidence of a passing perturbation of spacetime.

Four primary sources of gravitational waves are coalescing binary systems, pulsars, supernovae, and stochastic gravitational wave backgrounds (SGWB) [3]. We know that coalescing binary systems appear as "chirps". These chirps are the only signals we have detected so far. Pulsars should appear as sine waves due to their periodic emission of gravitational waves. Supernovae are extremely challenging sources to understand since we have yet to detect them, and parametrizing their signal in order to include them in matched filtering searches is unlikely. The fourth source, SGWBs, encompasses the unresolved gravitational wave sources. These unresolved sources include, for example, fluctuations from just after the Big Bang, as well as unresolved astrophysical sources like compact binary coalescences. "Stochastic" refers to a non-deterministic strain signal, either due to the generation process or detector limitations. The first three classes of GW sources act as the foreground to the fourth class of background that we are looking to fit and constrain. Because we do not have a deterministic signal that we can compare to the data to make a detection, we cross-correlate data to look for a common signal in multiple detectors.

Understanding the SGWB will help researchers probe the Universe earlier than electromagnetic signals currently allow [3]. Electromagnetic signals go back to about 400,000 years after the Big Bang, when scattering of particles decreased enough for photons to travel unimpeded. The SGWB could take us as far as 10^{-32} s after the Big Bang because GWs propagate through spacetime without the risk of scattering off particles [11]. For comparison, Planck Time is 5.39×10^{-44} s after the Big Bang. Thus, resolving the primordial background could help paint a clearer picture of the early Universe [10].

Determining a better and more general fit for the SGWB signal will also help us learn about the background itself [3]. As we add more time to our background detection survey, we will be able to resolve more features in the SGWB spectrum. The features in the SGWB spectrum will help us learn about the signals beyond the recognizable, precise events. As Allen [3] mentions, the more we record the signals on multiple detectors simultaneously, the better we will be able to transition the sources of the SGWB from "unresolved" to "resolved", allowing us to understand the astrophysical implications of the parameters we measure and constrain.

Additionally, developing better fits will help bound the stochastic background signal. Bounding the frequency ranges of key SWGB features, such as the energy spectrum turnover, will be helpful to deduce the components of this signal [13]. Our goal is to better constrain properties of the SGWB using available or future data. Current estimates from compact binary searches inform when we might make a GWB detection, but good SGWB parameter estimation can also be used to predict how many

CBCs we can detect in the future. These represent complementary efforts that may inform one another.

II. BUILDING THE SGWB SIGNAL

A. SGWB

Most models for a GWB predict a power-law spectrum, which is given by:

$$\Omega_{\rm GW}(f) = \Omega_{\rm ref}\left(\frac{f}{f_{\rm ref}}\right)^{\alpha}, \tag{1}$$

where $\Omega_{\rm GW}(f)$ is the energy density per logarithmic frequency interval used to describe the isotropic stochastic background. This quantity is physically defined as $\Omega_{\rm GW}(f) = \frac{f}{\rho_c}\frac{d\rho_{\rm GW}}{df}$ where ρ_c is the critical density and $\rho_{\rm GW}$ is energy density of gravitational waves in the infinitesimal frequency interval f to $f + df$ [3]. $\Omega_{\rm ref}$ is the the amplitude at a reference frequency, $f_{\rm ref}$. α is the spectral index. Both $\Omega_{\rm ref}$ and α are constrained using strain data. Right now, we can fit various parameter combinations for different frequency ranges of our spectrum [8].

B. BBH GWB

The energy density spectrum for a given BBH population is:

$$\Omega(f) = \frac{f}{\rho_c}\int dz \frac{\mathcal{R}(z)\langle\frac{dE}{df}|_{f(1+z)}\rangle}{(1+z)H(z)}. \tag{2}$$

$H(z)$ is the Hubble constant as a function of redshift. The $(1+z)$ factor in the denominator of the integral incorporates in the time delay of detecting redshifted objects. The population-averaged energy spectrum with respect to a BBH with object masses m_1 and m_2 is

$$\langle\frac{dE}{df}|_{f(1+z)}\rangle = \int dm_1 dm_2 \frac{dE}{df}(m_1, m_2; f(1+z))p(m_1, m_2) \tag{3}$$

and the merger rate density is:

$$\mathcal{R}(z) = \int dt_d R_*(z_f(z, t_d))F(Z \leq Z_c, z_f(z, t_d))p(t_d), \tag{4}$$

where t_d is the time delay [1]. $F(Z)$ is a function describing the metallicity weighting of the star formation rate, $R_*(z_f)$. To gain intuition on the impact of the metallicity on the BBH merger rate, suppose t_d is a fixed value for the time delay between the time of the merger and when it was detected. Then, the overall BBH $\mathcal{R}(z)$ will follow R_* with additional weighting by the metallicity at a given redshift. We weight the star formation rate by the metallicity to incorporate into the model that black holes are more likely to form in low metallicity environments.

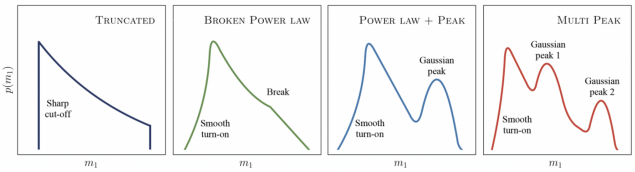

FIG. 1. Mass probability profiles. The assumed mass probability for varied $\mathcal{R}(z)$ is the third profile, power law + peak. The profile gives the probability of having a merger with each respective mass, independent of redshift. Figure from Ref. [2]

C. Mass Probability and Merger Rate Models

We will use an efficient technique to evaluate $\Omega_{GW}(f)$ given a model for the population of black holes and their merger rate with redshift. We discuss this below, but first we discuss the form of the mass distributions and merger rate models we plan to use. The mass probability distributions predominantly follow those in [2]. These four approximate mass probability forms (truncated, broken power law, power law + peak, multi peak) are shown in Fig. 1. We will default to the power law + peak profile when varying the merger density rate. The exact model and parameter posteriors that I utilize in my code analysis are also in [2]. For concision, I include the reference but not the extensive parameter posterior figures or tables.

We now consider the merger density rate. This profile is assumed to follow the star formation rate relatively closely, as previously described. One common form of the merger rate density that is used, because it is a good analytic description of estimates of the star formation rate, is given by [14]:

$$\mathcal{R}_{BBH}(z) = C(\lambda_1, \lambda_2, z_{peak})\frac{R_0(1+z)^{\lambda_1}}{1+\left(\frac{(1+z)}{(1+z_{peak})}\right)^{\lambda_1+\lambda_2}}, \tag{5}$$

where $C(\lambda_1, \lambda_2, z_{peak})$ is the normalization constant allowing $R_{BBH}(0) = R_0$, $R_0 = 31.88\ Gpc^{-3}yr^{-1}$ is the local merger density rate [12], z_{peak} is the location of the highest merger rate density in redshift space, λ_1 is the power law index up until z_{peak}, and λ_2 is the power law index after z_{peak}. Based on the initial value condition, we may manipulate λ_1, λ_2, and z_{peak} and look at the effect on $\Omega(f)$.

D. Number of Detectable Events

The number CBC events detectable using a typical matched-filter search, given R(z) is:

$$\int\left(\frac{dN}{dzdm}\right)dmdz = \int dmdz\frac{T_{obs}\mathcal{R}(z)\frac{dV}{dz}}{(1+z)}p(m)\eta(m, z). \tag{6}$$

We integrate over the $\mathcal{R}(z)$ curve itself converted from its volume density by expression $\frac{dV}{dz}$ and weighted by mass probability *p(m)* and detection efficiency $\eta(m,z)$. The multiplication of the integrand by factors T_{obs} and $(1+z)^{-1}$ converts the integral into a time-independent rate and account for the time delay, respectively. Probability weights *p(m)* are the same as the Power Law + Peak model shown in Fig. 1. Detection efficiencies $\eta(m,z)$ are generated in a grid by the BILBY Python Package. We write the cosmology-driven volume conversion as:

$$\frac{dV}{dz} = \frac{4\pi c\chi^2(z)}{(1+z)H_0E(z)} \tag{7}$$

where

$$\chi(z) = \frac{c}{H_0}\int \frac{dz}{E(z)} \tag{8}$$

and $E(z) = \sqrt{\Omega_m(1+z)^3+1-\Omega_m}$. In this work, we assume $\Omega_m = 0.3065$ and $H_0 = 69.32km/(Mpc\cdot s)$.

III. COMPUTATIONAL METHODS

A. RJMCMC

Three commonly used analytic models for the SGWB are as follows:

- Power Law: $\Omega_{\rm GW}(f) = \Omega_{\rm ref}\left(\frac{f}{f_{\rm peak}}\right)^{\alpha}$
- Broken Power law (BPL):
  $\Omega_{\rm GW}(f) = \begin{cases}\Omega_{\rm peak}(\frac{f}{f_{\rm peak}})^{\alpha_1} & \text{for } f \le f_{\rm peak}\\ \Omega_{\rm peak}(\frac{f}{f_{\rm peak}})^{\alpha_2} & \text{for } f > f_{\rm peak}\end{cases}$
- Smooth BPL:
  $\Omega_{\rm GW}(f) = \Omega_{\rm peak}(\frac{f}{f_{\rm peak}})^{\alpha_1}[1+(\frac{f}{f_{\rm peak}})^{\Delta}]^{(\alpha_2-\alpha_1)/\Delta}$

These models, although simplistic and described by few parameters which require fitting, are not as general and generic as we would like [9]. Alternative functional approaches include spline fitting. Spline fitting utilizes smooth, piece-wise polynomials of different degrees to describe a curve. Parameters come in the form of coefficients of a polynomial expansion:

$$p_j(x) = a_0 + a_1x + a_2x^2 + ... + a_nx^n \tag{9}$$

such that the a_i coefficients allow us to fit an n-degree polynomial to the curve segment j. This is advantageous where a single polynomial fit, such as attempting to use a single power law for the entire spectrum, fails. We will start with spline fitting to recover these parameters and their relationships to each other when constructing functional models for our data. In our SGWB analysis, we only require spline fit interpolations up to $n = 3$. The coefficients have no astrophysical meaning that we are aware of, but we can explore this further once confirming that cubic splines are a viable interpolator.

We propose the Westley fitting algorithm, which utilizes a combination of single power laws and splines to interpolate a fit between an optimized number of knots. Westley is a Reversible Jump Metropolis-Hastings Markov Chain Monte Carlo algorithm [7]. This means that a ratio of likelihoods between points drives the placement of knots in either the spline or power law fits. The term "Reversible Jump" means that the MCMC can propose adding or removing parameters from a model instead of just probing the existing parameters. First, a guess is made for the placement of the set of knots along a frequency interval. For now, this guess is made on a uniform prior over the local frequency bin. Next we calculate the likelihood of this knot configuration, which is a function of the cross-correlation between detectors and the model we have injected. We are essentially proposing to move a knot, interpolating between the knots to calculate the model, then using that knot-motivated model to calculate the likelihood of the data. We then propose to move the amplitude of a knot, add another knot, or remove a knot, and then calculate the likelihood again. If the likelihood of the second knot configuration is greater than the likelihood of the first knot placement, the second knot is kept. Otherwise, we throw out the second knot configuration and keep the first knot configuration. We repeat this process to form a chain, which should converge at a particular fit to the data.

An MCMC sampler such as Westley relies on the Metropolis-Hastings algorithm. In the following proposals, a set of equations is used to evaluate the likelihood of the proposal and the Hastings ratio, R. We define the acceptance probability for a new knot as:

$$P(m'|m) = min\left(1, \frac{p(m')}{p(m)}\frac{p(d|m')}{p(d|m)}\frac{q(m|m')}{q(m'|m)}\right). \tag{10}$$

$p(m)$ is the prior on model m, and $p(d|m)$ is the likelihood of the data given model m. Meanwhile, $q(m|m')$ is the ratio of probability of proposing to move from model m to model m'. The Hastings ratio, R, is embedded into the acceptance probability and is expressed as:

$$R = \frac{q(m|m')}{q(m'|m)}\frac{p(m')}{p(m)}. \tag{11}$$

The difference between the acceptance probability and the Hastings ratio lies in the ratio of the likelihoods for the two models.

For now, the Hastings ratios are consistently 1. However, in future Gaussian-based updates to the proposals, R will be more complicated, including a Gaussian exponential term. Future work will be deriving and implementing that expression.

B. Efficient Calculation of BBH Ω_{GW} Model

To avoid computing the 4D integral in Fig. 2, we utilize a matrix multiplication approximation presented by Tom Callister [5]. The computation of this integral occurs in two phases: the precomputation of an energy grid given mass and redshift values, followed by the calculation of the merger rate density as a function of redshift, z, and time delays, t_d. We may rewrite the population-averaged energy spectrum as a convolution of the radiated energy at every combination of masses, source redshifts, and frequencies with the probabilities over the mass grid given our population model:

$$\left\{\langle\frac{dE}{df}\rangle\right\}_{f,z} = \sum_{m_1,m_2}\left\{\frac{dE}{df}\right\}_{m_1,m_2,f,z}\{p\}_{m_1,m_2}. \quad (12)$$

The merger rate density becomes a grid of merger redshifts and time delays. The grid of formation redshifts is given as $\{z_f\}_{z,t_d}$. We distinguish between the source and detected reshifts and times due to the time delay of the CBC information reaching our detectors. We additionally utilize the star formation rate, $\{R_*\}_{z,t_d}$, a function we assume the merger rate follows. Finally, we combine these matrices with metallicity weights, $\{F\}_{z,t_d}$, representing the CBC formation as a function of redshift and time. The final expression for the merger rate density becomes:

$$\{\mathcal{R}\}_z = \sum_{t_d}(\{R_*\}_{z,t_d}\times\{F\}_{z,t_d})\{p\}_{t_d}. \quad (13)$$

Using these matrix multiplication approximations, instead of eqn. 2, we write:

$$\Omega(f) = \sum_z\left\{\frac{\mathcal{R}(z)}{(1+z)H(z)}\right\}_z\left\{\langle\frac{dE}{df}\rangle\right\}_{f,z}. \quad (14)$$

The independence of the two terms within the sum allows us to manipulate the merger rate density and energy spectrum independent of each other. In the next section, I will introduce how the various models for $\mathcal{R}(z)$ and $p(m)$ affect the $\Omega(f)$ spectrum.

IV. RESULTS & DISCUSSION

A. Parameter Variation

The first step of exploring the relationship between $\mathcal{R}(z)$ and $\Omega(f)$ is to vary the parameters of the merger density rate (eqn. 5) and map the effects onto $\Omega(f)$. Increasing z_{peak} alone results in much greater energy at low frequencies, as shown in Fig. 2. We expect this, since increasing z_{peak} alone also increases the area under the $\mathcal{R}(z)$ curve, implying more overall mergers which is effectively proportional to the amount of energy present.

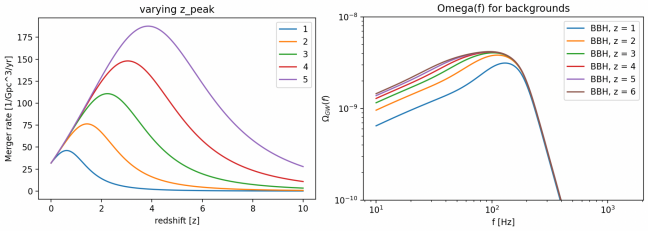

FIG. 2. Variance of only the z_{peak} parameter in $\mathcal{R}(z)$, leaving the spectral indices constant. The left plot shows the merger density rate profile for each z_{peak}. The right plot shows the corresponding $\Omega(f)$ for each varied $\mathcal{R}(z)$.

However, if we vary the location of the peak while attempting to conserve the area beneath $\mathcal{R}(z)$ as best as possible, we see effects on a different feature of the energy density spectrum than other parameter variations. Whereas the shift of z_{peak} alone caused the entire low frequency energy density to increase, horizontally shifting the peak location, as shown in Fig. 3, induces an energy density increase at the turnover in the BPL energy density spectrum. This effect agrees with less low-redshift mergers for higher z_{peak}, since those closer BBHs contribute greater to the energy density than high-redshift mergers.

Variation of spectral indices, λ_1 and λ_2, only changes the low frequency energy density before the turnover. This makes sense, since increasing the number of low-redshift BBHs adds energy to the system. In Fig. 4, the increase of λ_2 reduces the energy density at low frequencies. This is because cutting off high-redshift mergers and compressing the $\mathcal{R}(z)$ function at low redshifts reduces the overall BBHs allowed in the system, therefore lowering the total energy. Varying the parameters of $\mathcal{R}(z)$ within a reasonable range is a good way for building intuition of the effects of changing the BBH population concentrations at various redshifts on $\Omega(f)$.

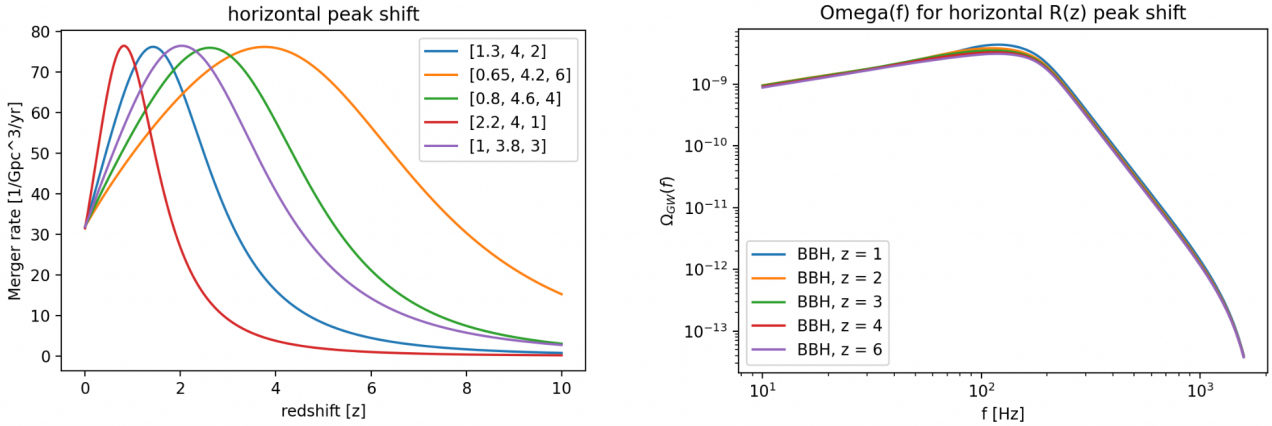

FIG. 3. Horizontal shifting of z_{peak} with corresponding changes in spectral indices λ_1 and λ_2. The legend refers to respective $[\lambda_1, \lambda_2, z_{peak}]$ values required to generate the respective $R_{BBH}(z)$ profiles. The left plot shows the merger density rate profile for each z_{peak}. The right plot shows the corresponding $\Omega(f)$ for each varied $\mathcal{R}(z)$.

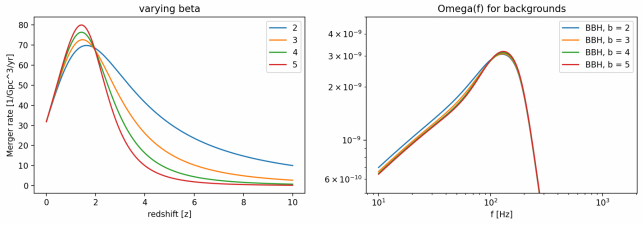

FIG. 4. Variance of only the λ_2 or β parameter in $\mathcal{R}(z)$, leaving the spectral indices constant. The left plot shows the merger density rate profile for each λ_2. The right plot shows the corresponding $\Omega(f)$ for each varied $\mathcal{R}(z)$.

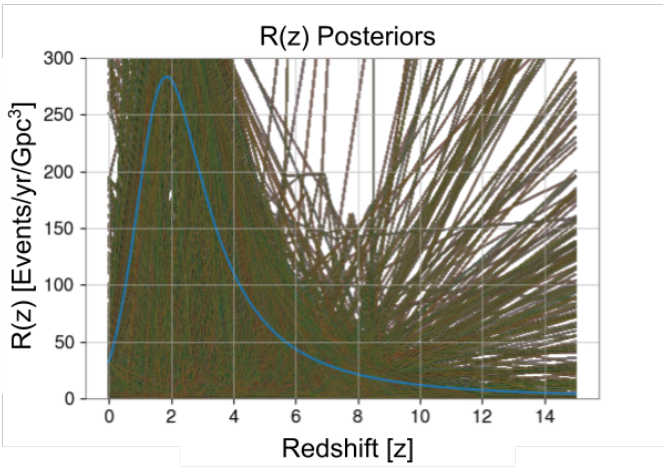

FIG. 5. Posterior fits for the injected $\mathcal{R}(z)$ (blue) utilizing Westley RJMCMC algorithm. Knots in this application of Westley are linearly interpolated.

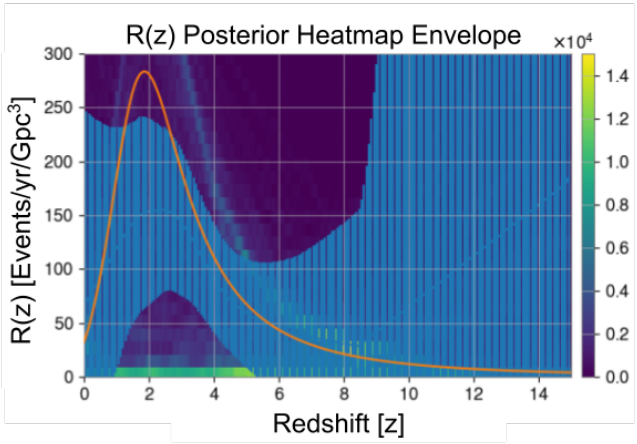

FIG. 6. The blue envelope encompasses the average posterior fit in redshift space up to 1σ of deviation. This envelope is overlaid on the heat map of fits to indicate the majority of the fits lie in the envelope region. The injected $\mathcal{R}(z)$ is in orange with primary spectral features corresponding to the envelope.

B. Fitting Merger Rate Distribution

While fitting $\Omega(f)$ allows us to measure or constrain the energy density spectrum of our GWB detections, we can also try to estimate the merger rate as a function of redshift for BBHs using the same fitting method. With a positive detection of $\Omega(f)$, we can constrain the merger rate, $\mathcal{R}(z)$ in redshift space.

We begin by initialising knots in the redshift space of $\mathcal{R}(z)$ instead of frequency space. This is an arbitrary placement in redshift space using randomized placement along uniform priors of the general shape of the suspected $\mathcal{R}(z)$. This is the same BBH merger density rate as a function of redshift utilised in eqn. 5. We then interpo-

late between these knots utilizing linear interpolation or cubic splines, depending on what we indicate to the fitter. The process of varying the knots is the same algorithm previously described.

Instead of then comparing the interpolated fit to the provided data, we calculate the $\Omega(f)$ using the interpolated $\mathcal{R}(z)$ using eqn. 2. The calculated energy density profile is compared to the data energy density profile. This comparison constructs the likelihood statistic used to either accept or reject the $\mathcal{R}(z)$ fit. We repeat this process for the specified number of iterations, for which we chose 100,000. In this case, we utilize the star formation rate (SFR) informed merger density rate. The SFR yields parameters $\alpha = 2.7$, $\beta = 2.9$, $z_{\rm peak} = 1.9$ that we inject into $\Omega(f)$. We then utilize Westley to recover these parameters from the calculated $\Omega(f)$ from this merger density rate (shown in blue in Fig. 5).

The posteriors of this abstracted fitting are shown in Fig. 5 in redshift space with calculated posteriors in frequency space shown in Fig. 8. We attribute the variation of energy spectrum posteriors in Fig. 8 to needing more iterations of Westley in future runs. Additionally, detector noise has greater energy than the GWB energy spectrum, which we consider in our analysis of the posteriors. In this run of the RJMCMC, we chose linear interpolation to minimize the divergence of the fits at high redshift. Fig. 5 is convoluted, so we superpose the posteriors as a heat map in Fig. 6. The lighter regions of the heat map reveal that using the RJMCMC in an alternate space from the data still returns key features of the parameter profile. For example, the spectral indices before and after the merger density peak are visually very similar to the blue injected $\mathcal{R}(z)$. Calculating the fits returns $z_{\rm peak} = 1.96 \pm 1.26$, which is consistent with the injected $z_{\rm peak} = 1.9$. Fig. 9 shows the histogram of merger density rate redshift peaks from the posteriors. We use eqn. 5 to find the parameters, namely z_{peak} for each posterior fit. We utilize built-in python curve-fitting to find the best parameters to fit Eqn. 5 to the posterior for each of the returned posteriors. The resulting z_{peaks} are then plotted on the histogram in Fig. 9. Since we are able to recover this key feature of the merger density rate, we conclude applying Westley in an alternate parameter space from the data is a viable approach for understanding the energy density spectrum and general application of Westley.

An alternative, more visual attestation to the generality of Westley is Fig. 6. The blue envelope overlaid with the heatmap encompasses 1σ from the average $\mathcal{R}(z)$ posterior fit. This is obtained by taking each vertical histogram of the heatmap and constructing a Gaussian. The $z_{\rm peak}$ value appears to be recovered by the envelope and the injected $\mathcal{R}(z)$ profile lies within the posterior envelope. The envelope is a good approximation for the merger density rate at low redshifts. We observe that as $z > 6$, the envelope diverges and oversaturates the posterior space. Better fitting at high redshift requires future work, since we need to apply boundary condition $R_{BBH}(z >> 1) \to 0$. An issue we encountered with spline and linear interpolation is the envelope divergence shown in Fig. 6. Despite, the behavior of the fits at high redshift, Westley recovers the low-redshift merger density rate features. This further reinforces the ability of the RJMCMC algorithm to recover astrophysical parameter profiles given a energy density profile. In this case, we knew the injected $\mathcal{R}(z)$, but the placement of knots in a different space from the data may help extract underlying relationships to obtained data.

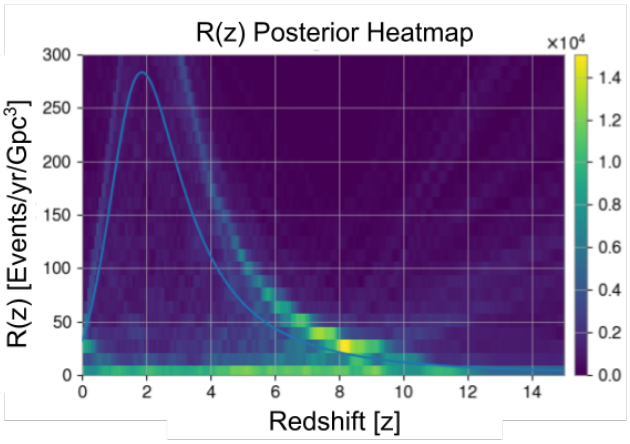

FIG. 7. The heatmap of posterior fits shown in Fig. 5. Lighter regions indicate more linearly interpolated fits running through that area of the heatmap. Spectral features matching the injected $\mathcal{R}(z)$ (blue) are evident on either side of $z_{\rm peak} = 1.9$. The lighter region along the horizontal axis is a consequence of the energy density spectrum noise exceeding the magnitude of the actual energy density spectral profile.

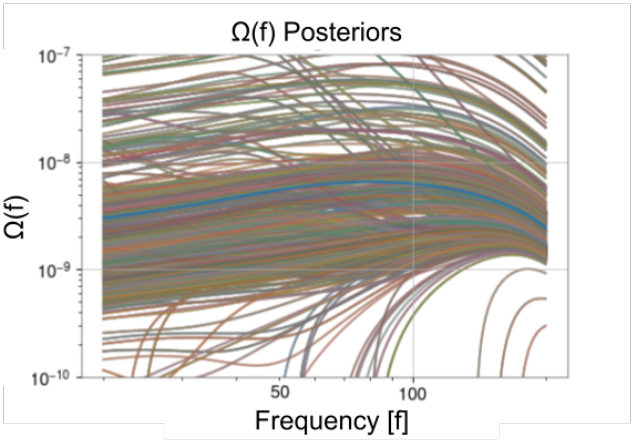

FIG. 8. The corresponding energy density spectral to the posterior $\mathcal{R}(z)$ shown in Fig. 5. These profiles are obtained by evaluating Eqn. 2 for the posterior $\mathcal{R}(z)$. The injected data $\Omega(f)$ is in blue.

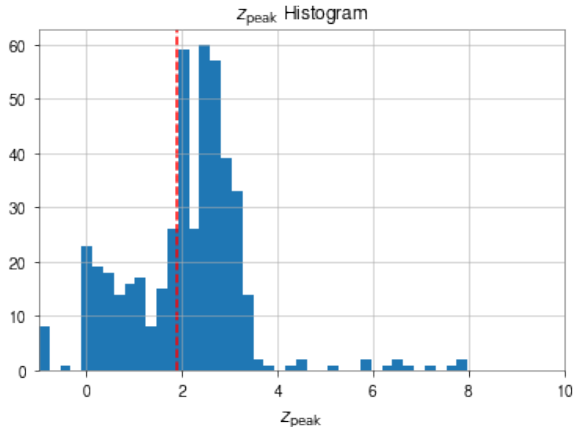

FIG. 9. The recovered z_{peak} values from the posterior $\mathcal{R}(z)$ fits in Fig. 5. The vertical red line is the injected $z_{\text{peak}} = 1.9$ from the SFR merger density rate. This histgram indicates the peak redshift of BBH merge density is recovered by the Westley fitting in redshift space given data in frequency space.

V. NEXT STEPS

There are a few potential next steps for applying both the Westley RJMCMC and merger rate density exploration. First, the Westley code can be packaged and cleaned up to operate as a pipeline. This is a versatile and generic tool for understanding parameter profiles and distributions that contribute to an energy density spectrum. Since not much prior knowledge is necessary to fit $\mathcal{R}(z)$ given an $\Omega(f)$, we can use this generalized fitter to learn about the distribution and characteristics of CBC's in our Universe that contribute to the GWB.

Similarly, we can push the fitting back another step and inject a Time Series instead of an $\Omega(f)$ data profile. This Time Series is a more realistic representation of the data, so we could investigate the effects of small changes to the merger density rate to what our interferometers see.

For Westley, it would also be productive to develop mechanisms of implementing stronger boundary conditions. Fig. 6 reveals a relatively consistent envelope about the injected merger density rate while $z < 6$. Once the redshift exceeds 6, the fits diverge where they should converge to 0. We know physically that there are a negligible number of mergers at high redshift due to the metallicity of the earlier universe. These diverging fits are evident in the individual posterior fits in Fig. 5, since the calculation itself knows there is little contribution to the overall energy density by high-redshift CBCs. Better understanding how to constrain the knots and fits in Westley will further Westley as a dependable fitter.

Overall, applying RJMCMC algorithms to data fitting is a new but hopeful approach. We expect this method to be more generic and general that previous fitting methods for GWB, which will give us more information about this elusive component of GW detection. As future detectors get more sensitive, we hope to use Westley to understand and fit the detections we make, making way for more knowledge about our early Universe.

VI. ACKNOWLEDGEMENTS

I'd like to thank Patrick Meyers and Arianna Renzini for their tremendous support in this project, as well as Tom Callister at UChicago for his astrophysical guidance and code. I'd like to thank the other LIGO Summer Undergraduate Research Fellows (SURFs) for their collaborative spirit and encouragement. I also gratefully acknowledge support from the National Science Foundation Research Experience for Undergraduates (NSF REU) program, California Institute of Technology, and LIGO Summer Undergraduate Research Fellowship.

[1] Benjamin P Abbott, Richard Abbott, TD Abbott, MR Abernathy, Fausto Acernese, Kendall Ackley, Carl Adams, Thomas Adams, Paolo Addesso, RX Adhikari, et al. Gw150914: Implications for the stochastic gravitational-wave background from binary black holes. Physical review letters, 116(13):131102, 2016.

[2] Rich Abbott, TD Abbott, S Abraham, F Acernese, K Ackley, A Adams, C Adams, RX Adhikari, VB Adya, Christoph Affeldt, et al. Population properties of compact objects from the second ligo–virgo gravitational-wave transient catalog. The Astrophysical journal letters, 913(1):L7, 2021.

[3] Bruce Allen. The stochastic gravity-wave background: sources and detection. In Relativistic Gravitation and Gravitational Radiation, Proceedings of the Les Houches School of Physics, held in Les Houches, Haute Savoie, volume 26, pages 373–418, 1997.

[4] Gregory Ashton, Moritz Hübner, Paul D Lasky, Colm Talbot, Kendall Ackley, Sylvia Biscoveanu, Qi Chu, Atul Divakarla, Paul J Easter, Boris Goncharov, et al. Bilby: A user-friendly bayesian inference library for gravitational-wave astronomy. The Astrophysical Journal Supplement Series, 241(2):27, 2019.

[5] Thomas Callister, Letizia Sammut, Shi Qiu, Ilya Mandel, and Eric Thrane. Limits of astrophysics with gravitational-wave backgrounds. Physical Review X, 6(3):031018, 2016.

[6] Eanna E Flanagan. Sensitivity of the laser interferometer gravitational wave observatory to a stochastic background, and its dependence on the detector orientations. Physical Review D, 48(6):2389, 1993.

[7] Peter J Green. Reversible jump markov chain monte carlo computation and bayesian model determination. Biometrika, 82(4):711–732, 1995.

[8] Vuk Mandic, Eric Thrane, Stefanos Giampanis, and Tania Regimbau. Parameter estimation in searches for the stochastic gravitational-wave background. Physical review letters, 109(17):171102, 2012.

[9] Katarina Martinovic, Patrick M Meyers, Mairi Sakellariadou, and Nelson Christensen. Simultaneous estimation of astrophysical and cosmological stochastic gravitational-wave backgrounds with terrestrial detectors. Physical Review D, 103(4):043023, 2021.

[10] Arianna I Renzini, Boris Goncharov, Alexander C Jenkins, and Patrick M Meyers. Stochastic gravitational-wave backgrounds: Current detection efforts and future prospects. Galaxies, 10(1):34, 2022.

[11] Joseph D Romano, Neil Cornish, et al. Detection methods for stochastic gravitational-wave backgrounds: a unified treatment. Living reviews in relativity, 20(1):1–223, 2017.

[12] Filippo Santoliquido, Michela Mapelli, Nicola Giacobbo, Yann Bouffanais, and M Celeste Artale. The cosmic merger rate density of compact objects: impact of star formation, metallicity, initial mass function, and binary evolution. Monthly Notices of the Royal Astronomical Society, 502(4):4877–4889, feb 2021.

[13] LIGO Scientific, BP Abbott, R Abbott, TD Abbott, S Abraham, F Acernese, K Ackley, C Adams, VB Adya, C Affeldt, et al. Search for the isotropic stochastic background using data from advanced ligo's second observing run. Physical Review D, 100(6):061101, 2019.

[14] LIGO Scientific and Virgo Collaboration. Upper limits on the isotropic gravitational-wave background from advanced ligo and advanced virgo's third observing run. Physical Review D Phys Rev D, 104(2):022004, 2021.

[15] Ashish Sharma and Jan Harms. Searching for cosmological gravitational-wave backgrounds with third-generation detectors in the presence of an astrophysical foreground. Physical Review D, 102(6):063009, 2020.